

**COMPUTATIONS OF PHASE CHANGE
FLOWS ON CURVED SURFACES USING
MULTI-DIRECTIONAL INTERFACE
CAPTURING METHODS**

ROHIT KUMAR



DEPARTMENT OF MECHANICAL ENGINEERING

INDIAN INSTITUTE OF TECHNOLOGY DELHI

JULY 2024

**COMPUTATIONS OF PHASE CHANGE
FLOWS ON CURVED SURFACES USING
MULTI-DIRECTIONAL INTERFACE
CAPTURING METHODS**

by

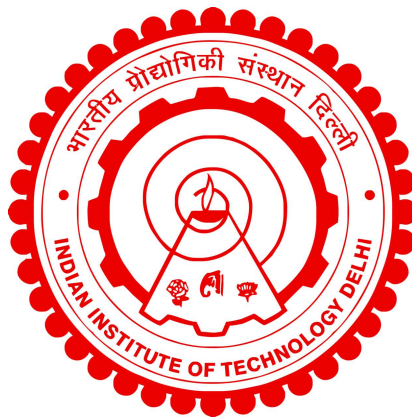
ROHIT KUMAR

DEPARTMENT OF MECHANICAL ENGINEERING

Submitted

in fulfillment of the requirements for the degree of Doctor of Philosophy

to the



INDIAN INSTITUTE OF TECHNOLOGY DELHI

JULY 2024

Dedicated to my beloved mother and younger brother

Certificate

This is to certify that the thesis entitled **Computations of Phase Change Flows on Curved Surfaces using Multi-directional Interface Capturing Methods**, being submitted by **Mr. Rohit Kumar** to the Indian Institute of Technology Delhi, for the award of the degree of **Doctor of Philosophy** in the Department of Mechanical Engineering is a bonafide record of the research work carried out by him under my guidance and supervision. To the best of my knowledge, the thesis has reached the requisite standard. We hereby declare that the content of the thesis, in full or in part, has not been submitted to any other Institute or University for the award of any degree or diploma.

Prof. B. Premachandran

Professor,

Department of Mechanical Engineering,

Indian Institute of Technology Delhi,

Hauz Khas, New Delhi-110016, India.

Date:

Place: New Delhi-110016,India.

Acknowledgements

I would like to express my deep sense of gratitude and indebtedness to my supervisor Prof. B. Premachandran for his illustrious guidance. His illustrious guidance, cooperation, coordination, encouraging interaction was the greatest driving force throughout my research work. His affectionate concern for students and his in depth appreciation of the problem at hand has kept him on a unique pedestal as an outstanding guide.

I would also like to express my sincere thanks to my senior research committee (SRC) members, Prof. Prabal Talukdar and Prof. Subhra Datta from the Department of Mechanical Engineering and Prof. Murali R. Cholemari from the Department of Applied Mechanics for their valuable suggestions during my research work.

I would like to express my gratitude to all research scholars of Heat and Mass Transfer lab especially Mr. S. M. Thamil Kumaran for constantly encouraging me.

Rohit Kumar

Abstract

The small spatial and temporal scales associated with boiling problems make experimental measurements very challenging. On the other hand, direct numerical simulations of boiling flow problems can resolve the small spatial and temporal scales associated with the problem. Therefore, in the past two decades many numerical models have been developed for simulating boiling flow problems. For modelling boiling flow problems, accurate interface capturing and accurate prediction of the interfacial heat and mass transfer is very important.

For numerical simulations of phase change problems, the front tracking method and the interface capturing methods are widely used. However, the front-tracking method is very challenging to implement for boiling flow problems as interface breakup, and merger is very common in boiling flow problems. Therefore, the interface capturing method is preferred for modelling boiling flow problems. The volume of fluid (VOF), the level set (LS), and the coupled level set and volume of fluid (CLSVOF) methods are the popular interface capturing methods preferred for simulating boiling flow problems. However, the use of the VOF method alone leads to unwanted spurious currents in the vicinity of the interface whereas the LS method suffers from the mass loss problem. Therefore, the CLSVOF method is preferred for the direct numerical simulation of boiling flow problems. However, most of the CLSVOF methods available in the literature use the operator-split advection method which is computationally expensive, as it requires interface reconstruction twice and thrice for 2D and 3D problems, respectively. Additionally, most of the numerical studies reported in the literature were performed using structured mesh. Hence, these studies were mostly limited to simple geometries. However, for real-life applications, geometries are complex, and it will be easy to mesh these geometries with unstructured meshes. Thus, in the present work, a CLSVOF method has been proposed for 3D unstructured polyhedral meshes with multi-directional advection. The proposed CLSVOF was thoroughly validated against a number of standard advection test cases. The interface error norms obtained using the proposed CLSVOF method compare well with the results available in the literature, which were obtained using higher-order interface reconstruction techniques. The accuracy and

performance of the proposed CLSVOF method were also checked for various two-phase flow test cases without phase change. Finally, the proposed CLSVOF method was used to simulate natural convection film boiling over a 3D flat surface and a 3D horizontal cylinder. The present heat transfer results are in good agreement with the results available in the literature.

Many analytical and experimental studies on flow film boiling over a sphere are available in the literature. However, most of these studies are focused on subcooled and saturated flow film boiling over a sphere in the natural and forced convection regime. For the natural convection regime, the effect of the surface tension force and the size of the heated spherical surface under reduced gravity levels is not very clear from the literature. Therefore, in the present work, the proposed multi-directional CLSVOF method was used to numerically study the effect of the size of the heated sphere on the interface evolution and the associated heat transfer characteristics for natural convection film boiling over a sphere under different gravity levels. For flow film boiling over a sphere, there is no proper heat transfer data available in the literature for the mixed convection regime as compared to the forced convection regime. Therefore, the proposed multi-directional CLSVOF method was used to numerically study flow film boiling over a sphere in the mixed convection regime. Simulations were performed for both the vertical and the horizontal flow configurations. The interface evolution, vapour wake dynamics, and heat transfer have been thoroughly investigated by varying the saturated liquid flow velocity, sphere diameter, and wall superheat for both flow configurations.

The experimental studies in the literature have reported that peculiar structures appear in the vapour film as the fluid approaches the critical pressure for film boiling over a wire. However, the exact physics behind this observation is not clearly explained in the literature. Therefore, this problem is studied numerically in the present work.

The mixed convection regime can also be important in some scenarios for film condensation over a bank of cylindrical tubes. However, the literature on condensation over a bank of cylindrical tubes in the mixed convection regime is very limited. Therefore, in the present work, the proposed multi-directional CLSVOF method was used to simulate flow film condensation over an inline arrangement of two cylinders in the mixed convection regime. The interface evolution and the associated

heat transfer characteristics were thoroughly studied by varying various flow and geometrical parameters. The condensate removal from the top cylinder was mostly observed to be in the form of individual droplets. However, a liquid column is formed between the two cylinders as condensate from the top cylinder gets drained to the second cylinder. The number of droplet generation sites was observed to increase as the cylinder diameter is increased. Interfacial waves were evident in the liquid film around the bottom cylinder for the large diameter cylinder. These interfacial waves significantly affect the heat transfer for the bottom cylinder. As the wall subcooling increases, the condensate removal pattern between the top cylinder and the bottom cylinder changes from a combination of liquid droplets and columns to stable liquid columns.

Finally, a new multi-directional advection method based moment of fluid (MOF) method developed for 2D unstructured mesh was extended to for 3D unstructured polyhedral mesh. The proposed multi-directional MOF method is computationally efficient and inexpensive than the multi-directional CLSVOF method proposed earlier in this work. The accuracy and performance of the proposed multi-directional MOF method were observed to be much better than the other multi-directional methods available in the literature.

सार

क्वथन समस्याओं से जुड़े छोटे स्थानिक और लौकिक पैमाने प्रयोगात्मक माप को बहुत चुनौतीपूर्ण बनाते हैं। दूसरी ओर, क्वथन प्रवाह समस्याओं के प्रत्यक्ष संख्यात्मक सिमुलेशन समस्या से जुड़े छोटे स्थानिक और लौकिक पैमानों को हल कर सकते हैं। इसलिए, पिछले दो दशकों में क्वथन प्रवाह समस्याओं के अनुकरण के लिए कई संख्यात्मक मॉडल विकसित किए गए हैं। क्वथन प्रवाह समस्याओं के मॉडलिंग के लिए, सटीक इंटरफ़ेस कैप्चरिंग और इंटरफ़ेसीय ऊष्मा और द्रव्यमान स्थानांतरण की सटीक भविष्यवाणी बहुत महत्वपूर्ण है।

चरण परिवर्तन समस्याओं के संख्यात्मक सिमुलेशन के लिए, फ्रंट ट्रैकिंग विधि और इंटरफ़ेस कैप्चरिंग विधियों का व्यापक रूप से उपयोग किया जाता है। हालाँकि, क्वथन प्रवाह समस्याओं के लिए फ्रंट-ट्रैकिंग विधि को लागू करना बहुत चुनौतीपूर्ण है क्योंकि क्वथन प्रवाह समस्याओं में इंटरफ़ेस ब्रेकअप और विलय बहुत आम है। इसलिए, क्वथन प्रवाह समस्याओं के मॉडलिंग के लिए इंटरफ़ेस कैप्चरिंग विधि को प्राथमिकता दी जाती है। द्रव की मात्रा (VOF), स्तर सेट (LS), और युग्मित स्तर सेट और द्रव की मात्रा (CLSVOF) विधियाँ लोकप्रिय इंटरफ़ेस कैप्चरिंग विधियाँ हैं जिन्हें क्वथन प्रवाह समस्याओं के सिमुलेशन के लिए प्राथमिकता दी जाती है। हालाँकि, अकेले VOF विधि के उपयोग से इंटरफ़ेस के आस-पास अवांछित नकली धाराएँ उत्पन्न होती हैं जबकि LS विधि द्रव्यमान हानि की समस्या से ग्रस्त है। इसलिए, क्वथन प्रवाह समस्याओं के प्रत्यक्ष संख्यात्मक सिमुलेशन के लिए CLSVOF विधि को प्राथमिकता दी जाती है। हालाँकि, साहित्य में उपलब्ध अधिकांश CLSVOF विधियाँ ऑपरेटर-विभाजन संवहन विधि का उपयोग करती हैं जो कम्प्यूटेशनल रूप से महंगी है, क्योंकि इसमें क्रमशः 2D और 3D समस्याओं के लिए दो बार और तीन बार इंटरफ़ेस पुनर्निर्माण की आवश्यकता होती है। इसके अतिरिक्त, साहित्य में रिपोर्ट किए गए अधिकांश संख्यात्मक अध्ययन संरचित जाल का उपयोग करके किए गए थे। इसलिए, ये अध्ययन अधिकतर सरल ज्यामिति तक ही सीमित थे। हालाँकि, वास्तविक जीवन के अनुप्रयोगों के लिए, ज्यामिति जटिल होती है, और इन ज्यामिति को असंरचित जालों के साथ जोड़ना आसान होगा। इस प्रकार, वर्तमान कार्य में, बहु-दिशात्मक संवहन के साथ 3D असंरचित बहुफलकीय जालों के लिए एक CLSVOF विधि प्रस्तावित की गई है। प्रस्तावित CLSVOF को कई मानक संवहन परीक्षण मामलों के विरुद्ध पूरी तरह से मान्य किया गया था। प्रस्तावित CLSVOF विधि का उपयोग करके प्राप्त किए गए इंटरफ़ेस त्रुटि मानदंड साहित्य में उपलब्ध परिणामों के साथ अच्छी तरह से मेल खाते हैं, जो उच्च-क्रम इंटरफ़ेस पुनर्निर्माण तकनीकों का उपयोग करके प्राप्त किए गए थे। प्रस्तावित CLSVOF विधि की सटीकता और प्रदर्शन को चरण परिवर्तन के बिना विभिन्न दो-चरण प्रवाह परीक्षण मामलों के लिए भी जाँचा गया।

अंत में, प्रस्तावित CLSVOF विधि का उपयोग 3D समतल सतह और 3D क्षैतिज सिलेंडर पर प्राकृतिक संवहन फिल्म उबलने का अनुकरण करने के लिए किया गया था। वर्तमान ऊष्मा स्थानांतरण परिणाम साहित्य में उपलब्ध परिणामों के साथ अच्छी तरह से मेल खाते हैं।

साहित्य में गोले पर फ्लो फिल्म क्वथन पर कई विश्लेषणात्मक और प्रायोगिक अध्ययन उपलब्ध हैं। हालाँकि, इनमें से अधिकांश अध्ययन प्राकृतिक और जबरन संवहन शासन में गोले पर उपशीतित और संतृप्त फ्लो फिल्म क्वथन पर केंद्रित हैं। प्राकृतिक संवहन शासन के लिए, कम गुरुत्वाकर्षण स्तरों के तहत सतह तनाव बल और गर्म गोलाकार सतह के आकार का प्रभाव साहित्य से बहुत स्पष्ट नहीं है। इसलिए, वर्तमान कार्य में, प्रस्तावित बहु-दिशात्मक CLSVOF विधि का उपयोग विभिन्न गुरुत्वाकर्षण स्तरों के तहत गोले पर प्राकृतिक संवहन फिल्म क्वथन के लिए इंटरफ़ेस विकास और संबंधित ऊष्मा हस्तांतरण विशेषताओं पर गर्म गोले के आकार के प्रभाव का संख्यात्मक रूप से अध्ययन करने के लिए किया गया था। गोले पर फ्लो फिल्म क्वथन के लिए, मजबूर संवहन शासन की तुलना में मिश्रित संवहन शासन के लिए साहित्य में कोई उचित ऊष्मा हस्तांतरण डेटा उपलब्ध नहीं है। इसलिए, मिश्रित संवहन शासन में गोले पर फ्लो फिल्म क्वथन का संख्यात्मक रूप से अध्ययन करने के लिए प्रस्तावित बहु-दिशात्मक CLSVOF विधि का उपयोग किया गया था। ऊर्ध्वाधर और क्षैतिज प्रवाह विन्यास दोनों के लिए सिमुलेशन किए गए थे। दोनों प्रवाह विन्यासों के लिए संतृप्त द्रव प्रवाह वेग, गोले के व्यास और दीवार के अतिताप को परिवर्तित करके इंटरफ़ेस विकास, वाष्प वेक गतिकी और ऊष्मा स्थानांतरण की गहन जांच की गई है।

साहित्य में प्रयोगात्मक अध्ययनों ने बताया है कि जब द्रव तार पर उबलने वाली फिल्म के लिए महत्वपूर्ण दबाव के करीब पहुंचता है, तो वाष्प फिल्म में अजीबोगरीब संरचनाएं दिखाई देती हैं। हालाँकि, इस अवलोकन के पीछे सटीक भौतिकी को साहित्य में स्पष्ट रूप से नहीं समझाया गया है। इसलिए, इस समस्या का वर्तमान कार्य में संख्यात्मक रूप से अध्ययन किया गया है।

मिश्रित संवहन व्यवस्था बेलनाकार नलियों के एक समूह पर फिल्म संघनन के लिए कुछ परिदृश्यों में भी महत्वपूर्ण हो सकती है। हालाँकि, मिश्रित संवहन व्यवस्था में बेलनाकार नलियों के एक समूह पर संघनन पर साहित्य बहुत सीमित है। इसलिए, वर्तमान कार्य में, मिश्रित संवहन व्यवस्था में दो सिलेंडरों की इनलाइन व्यवस्था पर प्रवाह फिल्म संघनन का अनुकरण करने के लिए प्रस्तावित बहु-दिशात्मक CLSVOF विधि का उपयोग किया गया था। विभिन्न प्रवाह और ज्यामितीय मापदंडों को बदलकर इंटरफ़ेस विकास और संबंधित ऊष्मा स्थानांतरण विशेषताओं का गहन अध्ययन किया गया। शीर्ष सिलेंडर से संघनन निष्कासन को अधिकतर व्यक्तिगत बूंदों के रूप में देखा गया। हालाँकि, दो सिलेंडरों के बीच एक

तरल स्तंभ बनता है क्योंकि शीर्ष सिलेंडर से संघनन दूसरे सिलेंडर में चला जाता है। सिलेंडर व्यास बढ़ने पर बूंद निर्माण स्थलों की संख्या में वृद्धि देखी गई। बड़े व्यास वाले सिलेंडर के लिए निचले सिलेंडर के चारों ओर तरल फिल्म में इंटरफेसियल तरंगें स्पष्ट थीं। ये इंटरफेसियल तरंगें निचले सिलेंडर के लिए ऊष्मा स्थानांतरण को महत्वपूर्ण रूप से प्रभावित करती हैं। जैसे-जैसे दीवार का उपशीतलन बढ़ता है, शीर्ष सिलेंडर और निचले सिलेंडर के बीच संघनन निष्कासन पैटर्न तरल बूंदों और स्तंभों के संयोजन से स्थिर तरल स्तंभों में बदल जाता है।

अंत में, 2D असंरचित मेस के लिए विकसित एक नई बहु-दिशात्मक संवहन विधि आधारित द्रव का क्षण (MOF) विधि को 3D असंरचित बहुफलकीय जाल के लिए विस्तारित किया गया। प्रस्तावित बहु-दिशात्मक MOF विधि इस कार्य में पहले प्रस्तावित बहु-दिशात्मक CLSVOF विधि की तुलना में कम्प्यू-टेशनल रूप से कुशल और सस्ती है। प्रस्तावित बहु-दिशात्मक MOF विधि की सटीकता और प्रदर्शन साहित्य में उपलब्ध अन्य बहु-दिशात्मक विधियों की तुलना में बहुत बेहतर पाया गया।

Contents

Certificate	i
Acknowledgements	ii
Abstract	iii
Contents	viii
List of Figures	xv
List of Tables	xxv
Nomenclature	xxvii
1 Introduction	1
1.1 Background	1
1.2 Two-phase flow modelling	5
1.2.1 Level set (LS) method	6
1.2.2 Volume of fluid (VOF) method	7
1.2.3 Coupled level set and volume of fluid (CLSVOF) method	8
1.2.4 Moment of fluid (MOF) method	8
1.3 Motivation for the present research work	9
1.4 Organisation of the thesis	9
2 Literature review	11
2.1 Introduction	11
2.2 Numerical modelling of two-phase flows	12
2.2.1 Moving mesh method	12
2.2.2 Front tracking method	12
2.2.3 Interface capturing method	13

2.2.3.1	Level set (LS) method	13
2.2.3.2	Volume of fluid (VOF) method	14
2.2.3.3	Coupled level set and volume of fluid (CLSVOF) method	17
2.2.3.4	Moment of fluid method	18
2.2.4	Direct numerical simulation of boiling flows	22
2.3	Film boiling over a sphere	26
2.4	Film boiling over a wire near the critical state	31
2.5	Film condensation over cylinders	34
2.6	Conclusions from the literature review	36
2.7	Objectives of the present research work	38
3	Development of a multi-directional CLSVOF method	41
3.1	Introduction	41
3.2	Mathematical formulation	42
3.2.1	Governing equations	42
3.2.2	Mass and energy jump across the interface	43
3.2.3	Interface capturing using the CLSVOF method	45
3.2.3.1	Interface advection	45
3.2.3.2	Interface reconstruction and re-initialization of level-set function	49
3.2.3.3	Surface tension force and interfacial properties	51
3.2.3.4	Interfacial cell temperature	52
3.2.3.5	Solution procedure	54
3.3	Validation of two-phase flow without phase change	56
3.3.1	Test cases for advection	56
3.3.1.1	2D translation test	57
3.3.1.2	2D Zalesak slotted disk test	58
3.3.1.3	2D vortex in a box test case	60
3.3.1.4	3D translation test	64
3.3.1.5	Sphere in a uniform flow	66
3.3.1.6	3D Zalesak sphere test	68
3.3.1.7	3D deformation test	71
3.3.2	Two-phase flow test cases	75
3.3.2.1	Static liquid drop	75
3.3.2.2	Rayleigh-Taylor instability	78
3.3.2.3	Two-dimensional rising bubble	83
3.3.2.4	Three-dimensional rising bubble	87
3.4	Validation of phase change problems	90
3.4.1	Stefan problem	90
3.4.2	Numerical simulation of boiling flows	92

3.4.2.1	Film boiling on a two-dimensional horizontal flat surface	93
3.4.2.2	Film boiling on a three-dimensional horizontal flat planar surface	99
3.4.2.3	Film boiling on a two-dimensional horizontal cylinder	104
3.4.2.4	Film boiling on a three-dimensional horizontal cylinder	109
3.5	Conclusion	116
4	Film boiling around a sphere: Part I-Natural convection regime	119
4.1	Introduction	119
4.2	Problem formulation	120
4.2.1	Computational domain and boundary conditions	120
4.2.2	Fluid properties	122
4.2.3	Simulation parameters	122
4.2.4	Mesh independence study and validation	123
4.3	Calculation of Nusselt number	125
4.4	Results and discussion	126
4.4.1	Effect of dimensionless sphere diameter	126
4.4.2	Effect of dimensionless wall superheat	136
4.4.3	Effect of external gravity field	144
4.4.4	Comparison of present numerical results with semi-empirical correlations	148
4.5	Conclusion	149
5	Film boiling around a sphere: Part II-Mixed and forced convection regime	151
5.1	Introduction	151
5.2	Problem formulation	154
5.2.1	Computational domain	154
5.2.2	Boundary and initial conditions	155
5.2.3	Nusselt number calculation	156
5.2.4	Fluid properties and simulation parameters	157
5.2.5	Grid independence study	158
5.2.6	Validation of the numerical model	159
5.3	Results and discussion	161
5.3.1	Effect of Reynolds number	162
5.3.2	Effect of dimensionless sphere diameter	177
5.3.3	Effect of dimensionless wall superheat	193
5.4	Conclusion	207
6	Film boiling over a wire	211
6.1	Introduction	211

6.2	Problem formulation	212
6.2.1	Computational domain and boundary conditions	212
6.2.2	Fluid properties and simulation parameters	212
6.3	Calculation of Nusselt number	212
6.3.1	Mesh independence study and validation	214
6.4	Results and discussion	215
6.5	Conclusion	220
7	Film condensation over an inline arrangement of two cylinders	223
7.1	Introduction	223
7.2	Problem formulation	224
7.2.1	Computational domain	224
7.2.2	Boundary and initial conditions	224
7.2.3	Nusselt number calculation	225
7.2.4	Fluid properties	226
7.2.5	Simulation parameters	226
7.2.6	Grid independence study	227
7.2.7	Validation	229
7.3	Results and discussion	230
7.3.1	Effect of pitch between the cylinders	230
7.3.2	Effect of cylinder diameter	237
7.3.3	Effect of the saturated vapour flow Reynolds number	246
7.3.4	Effect of degree of wall subcooling	255
7.4	Conclusion	261
8	Development of a multi-directional MOF method	265
8.1	Introduction	265
8.2	Interface capturing using the MOF method	266
8.2.1	Interface reconstruction	266
8.2.2	Multi-directional face-flux based advection	267
8.2.2.1	Geometric advection of zeroth moment (M_0)	268
8.2.2.2	Geometric advection of first moment (M_1)	271
8.2.3	Solution procedure	273
8.3	Validation studies	273
8.3.1	Advection test cases	273
8.3.1.1	3D deformation test case	274
8.3.1.2	3D Zalesak sphere test case	277
8.3.2	Two-phase flow without mass transfer	279
8.3.2.1	3D rising bubble test case	280
8.4	Film boiling and condensation studies	282
8.4.1	3D Free convection film boiling over a flat surface	282
8.4.2	3D Free convection film boiling over a cylinder	285

8.4.3	3D Free convection film condensation over a cylinder	290
8.5	Conclusion	295
9	Conclusion and suggestions for future work	297
9.1	Introduction	297
9.2	Major conclusions	299
9.3	Suggestions for future work	302
	Bibliography	305
	List of Publications	351
	Brief bio-data of the author	353

List of Figures

1.1	A typical boiling curve (Dhir, 1998).	2
1.2	Film boiling over a cylindrical heater (Liu and Theofanous, 1996). . .	3
1.3	Different methods used for direct numerical simulations of two-phase flows (Zhao et al., 2002). (a) Moving mesh method, (b) Interface tracking method and (c) Interface capturing method.	5
1.4	The two-phase interface in the level set method.	6
1.5	The two-phase interface in the volume of fluid method.	7
1.6	Comparison of the interface reconstruction in the VOF and MOF methods. (a) Original interface, (b) VOF-PLIC reconstruction and (c) MOF reconstruction.	8
3.1	A flux polyhedron truncated with the reconstructed interfacial plane.	48
3.2	A piecewise linear interface in a polyhedral cell.	50
3.3	E_1 error norm as a function of Courant number for the two-dimensional translation test case.	57
3.4	Interface profile obtained after one complete revolution in the two-dimensional slotted disk test case of Zalesak (Zalesak, 1979) for three different meshes (red: final shape, black: initial shape) (a) Structured mesh (b) Triangular mesh (c) Polyhedral mesh.	59
3.5	Results for time-dependent 2d vortex test for structured mesh.	61
3.6	Results for time-dependent 2d vortex test for unstructured triangular mesh.	62
3.7	Results for time-dependent 2d vortex test for unstructured polyhedral mesh.	62
3.8	Final interface shape for structured and successively refined polyhedral mesh.	63
3.9	Result for 2d vortex test of Balcázar et al. (2014).	63
3.10	E_1 error norm as a function of Courant number for simple translation of spherical fluid body.	65
3.11	Mesh as well as the 0.5 isocontour of the initial patched volume fraction data for sphere in a uniform flow.	66
3.12	Exact solution (red) and the 0.5 contour of final volume fraction data (a) Present work (b) Roenby et al. (2016).	67

3.13	Computational mesh for Zalesak slotted sphere rotation test. (a) Structured mesh (b) Unstructured mesh with tetrahedral cells (c) Unstructured mesh with polyhedral cells.	68
3.14	Results for Zalesak slotted sphere test case for structured mesh (1000000 hexahedral cells). (a) Initial interface (b) Final interface (c) Final interface of López and Hernández (2008).	69
3.15	Results for Zalesak slotted sphere test case for unstructured mesh. (a) Initial interface for the tetrahedral mesh (2295647 tetrahedral cells) (b) Final interface for the tetrahedral mesh (2295647 tetrahedral cells) (c) Final interface for the polyhedral mesh (787113 polyhedral cells) (d) Final interface for successively refined polyhedral mesh (2451267 polyhedral cells).	70
3.16	Results for 3D deformation test case for three different mesh at time instant $t = T/2, T$ with $T = 3$. (a) Structured mesh (2097152 cells) (b) Tetrahedral mesh (2795167 cells) (c) Polyhedral mesh (2983760 cells).	72
3.17	Results for 3D deformation test case on a Cartesian mesh of size $100 \times 100 \times 100$ at time instant $t = T/2, T$ with $T = 3$. (a) CLSVOF method of Wang et al. (2012) (b) General VOSET method of Cao et al. (2020) for curvilinear grid (c) Present CLSVOF method.	72
3.18	Pressure distribution and normalised pressure at $y = 0.5$ for 2D static bubble test case for different mesh configurations.	77
3.19	Zoomed view of the initial perturbation for Rayleigh-Taylor instability test. (a) Structured grid (b) Triangular grid (c) Polyhedral grid.	79
3.20	Deformed interface snapshots at different time instants for Rayleigh-Taylor instability test case. (a) Structured mesh (b) Polyhedral and Triangular mesh (c) Results of Zuzio and Estivalezes (2011).	80
3.21	Deformed interface snapshots at different time instants for 3D Rayleigh-Taylor instability test case.	82
3.22	Computational results of Haghshenas et al. (2017) for 3D Rayleigh-Taylor instability.	82
3.23	Set up and computational domain for the two-dimensional rising bubble test case.	84
3.24	Snapshots of two-dimensional bubble shapes at different time instants for different mesh configurations. (a) Structured mesh (b) Unstructured mesh (c) Polyhedral mesh.	85
3.25	Results for the two-dimensional rising bubble test case. (a) Rise velocity (v_c) (b) Circularity (ψ) (c) Bubble centroid (y_c).	86
3.26	Computational domain (a) and mesh (b) for the three-dimensional rising bubble test case.	87
3.27	2D and 3D images of the bubble interface at various time instants.	89
3.28	Temporal evolution of bubble rise velocity.	89
3.29	A schematic of Stefan problem.	90

3.30	Results of 1D Stefan problem (a) Interface position (b) Temperature profile	92
3.31	Snapshots of the vapour bubble development and pattern of their release for 2D film boiling on a horizontal flat surface (degree of wall superheat $\Delta T = 5$ K).	95
3.32	Time variation of space averaged Nusselt number for 2D film boiling on a flat surface.	96
3.33	Enlarged view of the vapour bubble formation for 2D film boiling on a flat surface for polyhedral mesh.	98
3.34	Snapshots of the vapour bubble development and pattern of their release for 2D film boiling on a flat surface for polyhedral mesh (degree of wall superheat $\Delta T = 5$ K).	98
3.35	Snapshots of the vapour bubble formation and release pattern for 3D film boiling over a flat plate for different wall superheats. (a) $\Delta T = 5$ K (b) $\Delta T = 10$ K.	101
3.36	Temperature contours for the cells containing the bubble for polyhedral mesh for $\Delta T = 10$ K. (a) Start of necking (b) just before pinch-off.	102
3.37	Time variation of space averaged Nusselt number for 3D film boiling over a flat plate for different wall superheats. (a) $\Delta T = 10$ K (b) $\Delta T = 20$ K.	103
3.38	Comparison of the present obtained time-averaged Nusselt numbers with the semi-empirical correlations of Berenson (1961) and Klimenko (1981) for different wall superheats.	104
3.39	The computational setup and zoomed view of the mesh around the heated cylinder for 2D film boiling over the cylinder.	105
3.40	Snapshots of the vapour bubble development and pattern of release for film boiling on a 2D horizontal cylinder for various wall superheats. (a) $\Delta T = 5$ K (b) $\Delta T = 10$ K.	107
3.41	Space averaged Nusselt number variation with time on a 2D cylinder for various wall superheats. (a) $\Delta T = 5$ K (b) $\Delta T = 10$ K.	108
3.42	The computational setup and the initial interface around the heated cylinder for 3D film boiling over the cylinder.	111
3.43	Snapshots of the vapour bubble formation and release pattern for 3D film boiling over a horizontal cylinder for $\Delta T = 10$ K.	113
3.43	<i>(continued)</i>	114
3.44	Space averaged Nusselt number variation with time on a 3D cylinder for various wall superheats. (a) $\Delta T = 5$ K (b) $\Delta T = 10$ K.	115
4.1	Schematic of the computational domain.	121
4.2	Schematic of the computational mesh.	124
4.3	Time evolution of the interface $D/\lambda_0 = 0.5$ and $Ja_v = 12.72$ at $g = 1.0g_e$	127

4.4	Time evolution of the interface for $D/\lambda_0 = 1.0$ and $Ja_v = 12.72$ at $g = 1.0g_e$	127
4.5	Velocity vector plot along with the instantaneous temperature distribution for $Ja_v = 12.72$ at $g = 1.0g_e$ in the x -plane. (a) $D/\lambda_0 = 0.5$ and (b) $D/\lambda_0 = 1.0$	128
4.6	Time evolution of the interface for $D/\lambda_0 = 5.0$ and $Ja_v = 12.72$ at $g = 1.0g_e$	129
4.6	(continued)	130
4.7	Velocity vector plot along with the instantaneous temperature distribution for $D/\lambda_0 = 5.0$ and $Ja_v = 12.72$ at $g = 1.0g_e$ in the x -plane.	131
4.8	Time variation of space averaged Nusselt number at $Ja_v = 12.72$ and $g = 1.0g_e$. (a) $D/\lambda_0 = 0.5$, (b) $D/\lambda_0 = 1.0$ and (c) $D/\lambda_0 = 5.0$. (d) Variation of space-time averaged Nusselt number with D/λ_0	133
4.9	Normalized FFT of the time variation of space averaged Nusselt number for saturated pool film boiling over a sphere of various diameters at $Ja_v = 12.72$ and $g = 1.0g_e$. (a) $D/\lambda_0 = 1.0$, (b) $D/\lambda_0 = 0.5$ and (c) $D/\lambda_0 = 5.0$	134
4.10	Interface profile for film boiling over a sphere just before bubble pinch-off for various diameters and at different dimensionless wall superheats and at $g = 1.0g_e$. (a) $D/\lambda_0 = 0.5$ and (b) $D/\lambda_0 = 1.0$	136
4.11	Time evolution of the interface for $D/\lambda_0 = 5.0$ and $Ja_v = 19.07$ at $g = 1.0g_e$	137
4.12	Comparison of the vapour waves on the interface for saturated pool film boiling over a sphere of dimensionless diameter $D/\lambda_0 = 5.0$ and $Ja_v = 19.07$ at $g = 1.0g_e$ with the results of Witte and Lienhard (1982) and Agaltsov et al. (2011).	138
4.13	Instantaneous streamlines near the interface for saturated pool film boiling over a sphere of dimensionless diameter $D/\lambda_0 = 5.0$ and $Ja_v = 19.07$ at $g = 1.0g_e$	139
4.14	Time variation of space averaged Nusselt number at $g = 1.0g_e$. (a) $D/\lambda_0 = 0.5$ and $Ja_v = 6.36$, (b) $D/\lambda_0 = 0.5$ and $Ja_v = 19.07$, (c) $D/\lambda_0 = 1.0$ and $Ja_v = 6.36$, (d) $D/\lambda_0 = 1.0$ and $Ja_v = 19.07$ and (e) $D/\lambda_0 = 5.0$ and $Ja_v = 19.07$. (f) Variation of space-time averaged Nusselt number with Ja_v	141
4.15	Normalized FFT of the time variation of space averaged Nusselt number for saturated pool film boiling over a sphere of various diameters and wall superheats at $g = 1.0g_e$	142
4.16	Time evolution of the interface for $D/\lambda_0 = 0.5$ and $Ja_v = 12.72$ and $g = 0.01g_e$	144
4.17	Time variation of the space averaged Nusselt number for $D/\lambda_0 = 0.5$ at $g = 0.01g_e$. (a) $Ja_v = 6.36$, (b) $Ja_v = 12.72$ and (c) $Ja_v = 19.07$	146

4.18	Normalized FFT of the time variation of space averaged Nusselt number for saturated pool film boiling over a sphere of the dimensionless diameter of $D/\lambda_0 = 0.5$ at $g = 0.01g_e$ but at different dimensionless wall superheats.	147
5.1	Schematic of the computational domain for forced flow film boiling on a sphere (a) vertical flow and (b) horizontal flow.	154
5.2	A typical computational grid used for film boiling simulations.	159
5.3	Interface evolution for the vertical flow configuration for $\tilde{D} = 1$ and $Ja^* = 0.6$ for various Re_D	163
5.4	Comparison of the present numerical result at $Re_D = 100$, $\sqrt{Fr} = 1.2$ for $\tilde{D} = 1$ and $Ja^* = 0.6$, with the conceptual illustration of Liu and Theofanous (1996) presented based on their experimental observation for completely saturated vertical flow film boiling on a sphere.	164
5.5	Interface evolution for the horizontal flow configuration for $\tilde{D} = 1$ and $Ja^* = 0.6$ at various Re_D	166
5.6	Interface evolution for the horizontal flow configuration for $\tilde{D} = 1$ and $Ja^* = 0.6$ at various Re_D	167
5.7	Variation of the dimensionless time-averaged vapour film thickness (τ_v/D) at the front stagnation point of the sphere versus Re_D at $Ja^* = 0.6$ and $\tilde{D} = 1$	169
5.8	Three-dimensional streamlines within the vapour wake for the vertical flow configuration at different Re_D for $\tilde{D} = 1$ and $Ja^* = 0.6$. (a) $Re_D = 50$ ($\sqrt{Fr} = 0.6$) and (b) $Re_D = 300$ ($\sqrt{Fr} = 3.6$).	170
5.9	Three-dimensional streamlines within the vapour wake for the horizontal flow configuration at different Re_D for $\tilde{D} = 1$ and $Ja^* = 0.6$. (a) $Re_D = 50$ ($\sqrt{Fr} = 0.6$) and (b) $Re_D = 300$ ($\sqrt{Fr} = 3.6$).	171
5.10	Two different views of the three-dimensional streamlines within the vapour wake, in the (x, y)-plane, for the horizontal flow configuration at $Re_D = 300$ ($\sqrt{Fr} = 3.6$) and $Ja^* = 0.6$ and $\tilde{D} = 1$. (a) first view and (b) second view.	172
5.11	Nusselt number at different Re_D for $\tilde{D} = 1$ and $Ja^* = 0.6$. (a) $Nu_{spaceAvg}$ versus time for vertical flow (b) $Nu_{spaceAvg}$ versus time for horizontal flow (c) $Nu_{timeAvg}$ versus Re_D	176
5.12	Interface evolution for the vertical flow configuration for $\tilde{D} = 5$ and $Ja^* = 0.6$ at various Re_D	178
5.13	Zoomed view of the thin vapour layer around the sphere for $\tilde{D} = 5$ and $Ja^* = 0.6$ at $Re_D = 50$ and 100.	179
5.14	Interface evolution for the vertical flow configuration for $\tilde{D} = 0.5$ and $Ja^* = 0.6$ at Re_D of 50 and 300.	181
5.15	Interface evolution for the horizontal flow configuration for $\tilde{D} = 5$ and $Ja^* = 0.6$ at $Re_D = 300$, $\sqrt{Fr} = 0.3$	183

5.16	Zoomed views of the evolving interface for the horizontal flow film boiling on a sphere for $\tilde{D} = 5$ and $Ja^* = 0.6$ at $Re_D = 300$, $\sqrt{Fr} = 0.3$.	183
5.17	Interface evolution for the horizontal flow configuration for $\tilde{D} = 0.5$ and $Ja^* = 0.6$ at different Re_D .	185
5.18	Variation of τ_v/D versus \tilde{D} at different Re_D at $Ja^* = 0.6$ for both the vertical and horizontal flow configurations.	186
5.19	Three-dimensional streamlines within the vapour wake for the vertical flow configuration at $Re_D = 300$, $\sqrt{Fr} = 0.3$ for $\tilde{D} = 5$ and $Ja^* = 0.6$.	187
5.20	Three-dimensional streamlines within the vapour wake for the vertical flow configuration at $Re_D = 300$, $\sqrt{Fr} = 10.25$ for $\tilde{D} = 0.5$ and $Ja^* = 0.6$.	187
5.21	Three-dimensional streamlines within the vapour wake for the horizontal flow configuration for $\tilde{D} = 0.5$ at different Re_D for $Ja^* = 0.6$. (a) $Re_D = 50$ and (b) $Re_D = 300$.	189
5.22	Three-dimensional streamlines within the vapour wake for the horizontal flow configuration for $\tilde{D} = 5$ at $Re_D = 300$, $\sqrt{Fr} = 0.3$ and $Ja^* = 0.6$.	190
5.23	Nusselt numbers for $\tilde{D} = 0.5$ and 5 at different Re_D and $Ja^* = 0.6$. (a) and (b) $Nu_{spaceAvg}$ versus time for $\tilde{D} = 0.5$ and 5 for different Re_D for vertical flow, (c) and (d) $Nu_{spaceAvg}$ versus time for $\tilde{D} = 0.5$ and 5 for different Re_D for horizontal flow, (e) $Nu_{timeAvg}$ versus \tilde{D} for different Re_D .	191
5.24	Interface evolution for the vertical flow configuration for $\tilde{D} = 1$ and $Re_D = 50$, $\sqrt{Fr} = 0.6$ at different wall superheats. (a) $Ja^* = 0.3$ and (b) $Ja^* = 0.9$.	194
5.25	Three-dimensional streamlines within the vapour wake for the vertical flow configuration for $\tilde{D} = 1$ at $Re_D = 50$, $\sqrt{Fr} = 0.6$ at different wall superheats. (a) $Ja^* = 0.3$ and (b) $Ja^* = 0.9$.	195
5.26	Temperature distribution within the vapour for $\tilde{D} = 1$ at $Re_D = 50$, $\sqrt{Fr} = 0.6$ at different wall superheats. (a) $Ja^* = 0.3$ and (b) $Ja^* = 0.9$.	196
5.27	Interface evolution for the horizontal flow configuration for $\tilde{D} = 1$ and $Re_D = 50$, $\sqrt{Fr} = 0.6$ at different wall superheats. (a) $Ja^* = 0.3$ and (b) $Ja^* = 0.9$.	198
5.28	Three-dimensional streamlines within the vapour wake for the horizontal flow configuration for $\tilde{D} = 1$ at $Re_D = 50$, $\sqrt{Fr} = 0.6$ at different wall superheats. (a) $Ja^* = 0.3$ and (b) $Ja^* = 0.9$.	200
5.29	Variation of τ_v/D versus Ja^* at $\tilde{D} = 1$ and $Re_D = 50$ for both the vertical and horizontal flow configurations.	201
5.30	Temperature distribution within the vapour for $\tilde{D} = 1$ at $Re_D = 50$, $\sqrt{Fr} = 0.6$ at different wall superheats. (a) $Ja^* = 0.3$ and (b) $Ja^* = 0.9$.	201

5.31	Nusselt numbers for $\tilde{D} = 1$ at various Re_D and Ja^* . (a) and (b) $Nu_{spaceAvg}$ versus time for $\tilde{D} = 1$ for different Re_D and $Ja^* = 0.3, 0.9$ for vertical flow, (c) $Nu_{spaceAvg}$ versus time for $\tilde{D} = 1$ for different Re_D and $Ja^* = 0.9$ for horizontal flow, (e) $Nu_{timeAvg}$ versus Re_D for $\tilde{D} = 1$ at different Ja^*	203
5.32	FFT of $Nu_{spaceAvg}$ for the vertical flow configuration.	204
5.33	FFT of $Nu_{spaceAvg}$ for the horizontal flow configuration.	205
6.1	Schematic of the computational domain.	213
6.2	An enlarged view of the computational mesh around the heated cylindrical wire.	214
6.3	Interface evolution pattern for film boiling of water at near critical pressure over a cylindrical wire at $T_{sat} = 646.55$ K and $T_{sup} = 11.76$ K at $t = 0.326$ s.	216
6.4	Enlarged view of the temperature distribution along with the line integral convolution of the velocity field for film boiling of water at near critical pressure over a cylindrical wire at $T_{sat} = 646.55$ K and $T_{sup} = 11.76$ K at $t = 0.326$ s.	216
6.5	Interface evolution pattern for film boiling of water at near critical pressure over a cylindrical wire at $T_{sat} = 646.91$ K and $T_{sup} = 3.0$ K at $t = 0.529$ s.	217
6.6	Enlarged view of the temperature distribution along with the line integral convolution of the velocity field for film boiling of water at near critical pressure over a cylindrical wire at $T_{sat} = 646.91$ K and $T_{sup} = 3.0$ K at $t = 0.529$ s.	218
6.7	An enlarged view of the interface of the mushroom-shaped vapour bubbles along with the planar streamlines coloured based on the vorticity field.	219
7.1	Schematic of the computational domain.	225
7.2	A typical computational grid used for the present simulations.	228
7.3	Interface evolution for $\tilde{P} = 2.8$, $Re_v = 100$, $Ja_l = 1.736$ and $\hat{D} = 1$	230
7.4	Interface evolution for $\tilde{P} = 4.2$, $Re_v = 100$, $Ja_l = 1.736$ and $\hat{D} = 1$	231
7.5	Interface evolution for $\tilde{P} = 5.6$, $Re_v = 100$, $Ja_l = 1.736$ and $\hat{D} = 1$	232
7.6	Temperature distribution along with the line integral convolution of the velocity field for $\tilde{P} = 2.8$, $Re_v = 100$, $Ja_l = 1.736$ and $\hat{D} = 1.0$	233
7.7	Temperature distribution along with the line integral convolution of the velocity field for $\tilde{P} = 4.2$, $Re_v = 100$, $Ja_l = 1.736$ and $\hat{D} = 1.0$	234
7.8	Temperature distribution along with the line integral convolution of the velocity field for $\tilde{P} = 5.6$, $Re_v = 100$, $Ja_l = 1.736$ and $\hat{D} = 1.0$	235
7.9	Variation of $Nu_{time,avg}$ with \tilde{P} for $Re_v = 100$, $Ja_l = 1.736$ and $\hat{D} = 1$	236
7.10	Interface evolution for $\tilde{P} = 4.2$, $Re_v = 100$, $Ja_l = 1.736$ and $\hat{D} = 5.0$	238

7.11	A qualitative comparison of the present interface (enlarged view) at $\tilde{P} = 4.2$, $Re_v = 100$, $Ja_l = 1.736$ and $\hat{D} = 5.0$ with the experimental results of Honda et al. (1989). (a) Present numerical result and (b) experimental result of Honda et al. (1989).	240
7.12	Temperature distribution along with line integral convolution of the velocity field for $\tilde{P} = 4.2$, $Re_v = 100$, $Ja_l = 1.736$ and $\hat{D} = 5.0$	241
7.13	Interface evolution for $\tilde{P} = 4.2$, $Re_v = 100$, $Ja_l = 1.736$ and $\hat{D} = 0.5$	242
7.14	Temperature distribution along with the line integral convolution of the velocity field for $\tilde{P} = 4.2$, $Re_v = 100$, $Ja_l = 1.736$ and $\hat{D} = 0.5$ at $t = 0.140s$	243
7.15	Enlarged view of the temperature distribution along with the velocity vector plot within the liquid film formed between the cylinders in the mid (y, z)-plane for $\tilde{P} = 4.2$, $Re_v = 100$, $Ja_l = 1.736$ and $\hat{D} = 0.5$	244
7.16	Variation of $Nu_{time,avg}$ with \hat{D} for $\tilde{P} = 4.2$, $Re_v = 100$ and $Ja_l = 1.736$	245
7.17	Interface evolution for $\tilde{P} = 5.6$, $Re_v = 25$, $Ja_l = 1.736$ and $\hat{D} = 1.0$	247
7.18	Interface evolution for $\tilde{P} = 5.6$, $Re_v = 150$, $Ja_l = 1.736$ and $\hat{D} = 1.0$	248
7.19	Temperature distribution along with line integral convolution of the velocity field for $\tilde{P} = 5.6$, $Re_v = 25$, $Ja_l = 1.736$ and $\hat{D} = 1.0$	249
7.20	Temperature distribution along with line integral convolution of the velocity field for $\tilde{P} = 5.6$, $Re_v = 150$, $Ja_l = 1.736$ and $\hat{D} = 1.0$	250
7.21	Zoomed view of the liquid column developed in the wake of the bottom cylinder for $\tilde{P} = 5.6$, $Re_v = 25$, $Ja_l = 1.736$ and $\hat{D} = 1.0$	251
7.22	Zoomed view of the liquid column developed in the wake of the bottom cylinder for $\tilde{P} = 5.6$, $Re_v = 150$, $Ja_l = 1.736$ and $\hat{D} = 1.0$	251
7.23	Three-dimensional streamlines in the vicinity of the liquid column developed in the wake of the bottom cylinder for $\tilde{P} = 5.6$, $Re_v = 25$, $Ja_l = 1.736$ and $\hat{D} = 1.0$	252
7.24	Three-dimensional streamlines in the vicinity of the liquid column developed in the wake of the bottom cylinder for $\tilde{P} = 5.6$, $Re_v = 150$, $Ja_l = 1.736$ and $\hat{D} = 1.0$	253
7.25	Variation of $Nu_{time,avg}$ with Re_v for $\tilde{P} = 5.6$, $Ja_l = 1.736$ and $\hat{D} = 1.0$	254
7.26	Interface evolution for $\tilde{P} = 4.2$, $Re_v = 25$ and $\hat{D} = 1.0$ for different Ja_l	256
7.27	Temperature distribution along with the line integral convolution of the velocity field for $\tilde{P} = 4.2$, $\hat{D} = 1.0$, $Ja_l = 1.736$ and $Re_v = 25$	257
7.28	Temperature distribution along with the line integral convolution of the velocity field for $\tilde{P} = 4.2$, $\hat{D} = 1.0$, $Ja_l = 3.472$ and $Re_v = 25$	258
7.29	Temperature distribution along with the line integral convolution of the velocity field for $\tilde{P} = 4.2$, $\hat{D} = 1.0$, $Ja_l = 5.208$ and $Re_v = 25$	259
7.30	Variation of $Nu_{time,avg}$ with Ja_l for $\tilde{P} = 4.2$, $\hat{D} = 1.0$ and $Re_v = 25$	260
8.1	Volume conserved flux polyhedron construction.	269
8.2	Subdivided polyhedron.	270

8.3	Advection of first moment through face ab of a 2D cell $abcd$ (Thamil Kumaran, 2024).	271
8.4	Comparison of the interfaces at $t = T/2$ and T for the 3D deformation test case on a structured mesh of size $128 \times 128 \times 128$. (a) Present MOF result, (b) MOF result of Mukundan et al. (2022) and (c) CLSVOF result of Mukundan et al. (2022).	276
8.5	Interface evolution of the spherical fluid element in the 3D deformation test case for an unstructured polyhedral mesh obtained from the proposed MOF method.	276
8.6	The initial and final interfaces for the 3D Zalesak sphere test case on structured mesh. (a) Initial interface, (b) Interface after one rotation (proposed MOF method), (c) Interface after one rotation from the present CLSVOF method and (d) Interface after one rotation for the VOF method of López and Hernández (2008).	278
8.7	(a) The initial interface and (b) the final interface obtained from the present MOF method for the 3D Zalesak sphere test case on unstructured mesh.	278
8.8	Interface evolution for the 3D rising bubble test case at $Re = 9.8$	280
8.9	Bubble rise velocity for the 3D rising bubble test case.	281
8.10	Interface evolution for film boiling of water over a 3D flat surface.	283
8.11	Temporal evolution of $Nu_{s,Avg}$ for film boiling over a 3D flat surface. (a) $\Delta T = 5.0$ K, (b) $\Delta T = 10.0$ K and (c) $\Delta T = 15.0$ K.	284
8.12	Comparison of the present $Nu_{st,Avg}$ values obtained for film boiling over a 3D flat surface at different ΔT with the results available in the literature.	285
8.13	A schematic of the computational domain used for film boiling over a 3D cylinder.	286
8.14	Interface evolution for film boiling over a cylinder. (a) $\Delta T = 10.0$ K and (b) $\Delta T = 15.0$ K.	287
8.15	Temporal evolution of $Nu_{s,Avg}$ for film boiling over a cylinder. (a) $\Delta T = 5.0$ K, (b) $\Delta T = 10.0$ K and (c) $\Delta T = 15.0$ K.	289
8.16	Present $Nu_{st,Avg}$ values compared with the results available in the literature.	290
8.17	A schematic of the domain used in the present study.	291
8.18	Interface evolution for film condensation of R123 over a cylinder. (a) $\Delta T = 3.0$ K, (b) $\Delta T = 6.0$ K and $\Delta T = 9.0$ K.	292
8.19	Temporal evolution of $Nu_{s,Avg}$ for film condensation of R123 over a cylinder. (a) $\Delta T = 3.0$ K, (b) $\Delta T = 6.0$ K and (c) $\Delta T = 9.0$ K.	294
8.20	Comparison of the present $Nu_{st,Avg}$ values obtained for film condensation over a cylinder at different wall subcooling with the results available in the literature.	294

List of Tables

3.1	E_2 error norm for 2d slotted disk test case.	60
3.2	E_1 error norm for 2d vortex in a box test case.	64
3.3	E_1 error norm for 3d sphere in a uniform flow with unstructured mesh.	67
3.4	E_1 error norm for Zalesak slotted sphere in a uniform vorticity field.	70
3.5	E_1 error norm for 3D deformation test case.	74
3.6	Typical errors for the static drop test case.	78
3.7	Physical properties of water at $P_{sat} = 21.9$ MPa and $T_{sat} = 646$ K. ($\sigma = 0.07$ mN/m, $h_{lg} = 276.4$ kJ/kg)	93
3.8	Nusselt number comparison for 2D film boiling on a horizontal flat surface.	99
3.9	Comparison of time-averaged Nusselt number for 2D film boiling on a horizontal cylinder for different values of wall superheats.	110
3.10	Comparison of the time-averaged Nusselt number for 3D film boiling on a horizontal cylinder for different values of wall superheats.	115
4.1	Physical properties of water at $T_{sat} = 646$ K and $P_{sat} = 21.9$ MPa. ($\sigma = 0.00007$ N/m, $h_{lv} = 276400$ J/kg)	122
4.2	Details of the grid independence test.	125
4.3	Comparison of present heat transfer results with the semi-empirical correlations for saturated pool film boiling over a sphere under normal gravity condition.	148
5.1	Details of the grid independence study.	158
5.2	Validation of the present numerical results against the experimental results of Sakurai et al. (1990).	160
5.3	Validation of the present numerical results against the experimental results of Liu and Fukuda (2008).	161
5.4	The corresponding values of \sqrt{Fr} for different \tilde{D} and Re_D	179
6.1	Details of the grid independence test.	215
7.1	Thermophysical properties of refrigerant R-123 at $T_s = 455.8$ K and $P_{sat} = 3.6$ MPa. ($\sigma = 0.0307$ mN/m, $h_{lv} = 25.4$ kJ/kg)	226
7.2	Details of the grid independence study.	229

8.1	For the 3D deformation test case, the L_1 error norm.	277
8.2	For the 3D Zalesak sphere test case, the L_1 error norm	279
8.3	Fluid properties of water at 21 900 kPa and 646.0 K ($h_{lg} = 276\,400$ J/kg, $\sigma = 0.000\,07$ N/m,).	286
8.4	Fluid properties of R123 at a pressure of 3.6 MPa and temperature 455.8 K. ($\sigma = 0.0307$ mN/m, $h_{lg} = 25.4$ kJ/kg)	291

Nomenclature

Alphabetical

\vec{V}	Velocity, [m/s]
\vec{V}_I	Interface velocity, [m/s]
\vec{V}_{mt}	Interface velocity due to mass transfer, [m/s]
v_c, V_c	Volume of the computational cell, [m ³]
V_f	Volumetric flux through a face, [m ³]
v_{fl}	Net fluid volume leaving a mixed cell, [m ³]
V_d	Advected volume, [m ³]
V_p	Flux polyhedron volume, [m ³]
p	Pressure, [Pa]
F_s	Volumetric surface tension force, [N/m ³]
\vec{g}, g, g_e	Gravitational constant, [m ² /s]
C_p	Specific heat at constant pressure, [J/kg · K]
T	Temperature, [K]
k	Thermal conductivity, [W/m · K]
\dot{m}	Interfacial mass flux, [kg/m ² · s]
q_I	Interfacial heat flux, [W/m ²]
q_n	Normal heat flux, [W/m ²]
t	time, [s]
Δt	time step size, [s]
h_{lg}	Latent heat, [J/kg]
H	Heaviside function
Nu	Nusselt number
h	Characteristic cell size
u, v, w	x,y and z velocity components, [m/s]
p/p_c	Pressure ratio
p_t	Pitch between the cylinders, [m]

Fr	Froude number
D	Diameter, [m]
D_{vb}	Vapour bubble diameter, [m]
U_∞	Free-stream velocity, [m/s]
\bar{h}	Average heat transfer coefficient, [W/m ² · K]
N	Number of cylindrical tubes
\hat{n}	Interface unit normal vector
\hat{n}_{f_e}, \hat{n}_f	Face unit normal vector
S_f	Face area, [m ²]
Re	Reynolds number
EO	Eötvös number
M	Morton number
Gr	Grashof number
Pr	Prandtl number
Ja	Jacob number
Bo	Bond number
d_b/D	Dimensionless departure bubble diameter, [m]
\mathcal{M}_0	Zeroth moment of fluid
\mathcal{M}_1	Second moment of fluid
\mathbf{x}_Ω	Fluid centroid
$area$	Area, [m ²]

Greek symbols

ρ	Density, [kg/m ³]
τ	Stress tensor
σ	Coefficient of surface tension, [N/m]
κ	Interfacial curvature, [m ⁻¹]
δ	Dirac delta function
α	Volume fraction
α_{mt}	Rate of generation of volume fraction
ϕ	Level set function
μ	Viscosity, [Pa · s]
ϵ	Emissivity
σ_{SB}	Stefan-Boltzmann constant, [W/m ² · K ⁴]
τ_v	time-averaged vapour film thickness at the front stagnation point

θ_s	flow separation angle
λ_0	Capillary length scale, [m]
λ_c	Critical wavelength, [m]
λ_d	Most dangerous wavelength, [m]

Superscripts

$n + 1$	present time step
n	previous time step

Subscripts

I	Interface
l	Liquid phase
g	Vapour phase
sat	Saturation
sup	Superheat
sub	Subcooling
avg	Average
$quad$	Quadilateral cells
$w, wall$	wall

Acronyms

VOF	Volume of fluid
FT	Front tracking method
LS	Level set method
CLSVOF	Coupled level set and volume of fluid method
MOF	Moment of fluid method
Str	Structured mesh
Unstr	Unstructured mesh
PF	Phase field method
CICS	Compressive high-resolution interface capturing scheme
CSF	Continuum surface force
HPC	High performance computing
MPI	Message passing interface
PLIC	Piecewise linear interface calculation
EMFPA	Edge matched flux polygon advection

FMFPA	Face matched flux polygon advection
ELVIRA	Efficient least squares volume of fluid interface reconstruction algorithm
PROST	Parabolic reconstruction of surface tension
SIR	Spline interface reconstruction
QUASI	Quadratic spline interface reconstruction
VOSET	Coupled volume of fluid and level set method
AMR	Adaptive mesh refinement
EI-LE	Eulerian-implicit and Lagrangian-explicit
CLSMOF	Coupled level set and moment of fluid method
IDW	Inverse Distance Weighted
GMRES	Generalized minimal residual method
FFT	Fast-Fourier transform